

7-2-2018

Covalency is Frustrating: La₂Sn₂O₇ and the Nature of Bonding in Pyrochlores under High Pressure–Temperature Conditions

Christian Childs
University of Nevada, Las Vegas

Keith V. Lawler
University of Nevada, Las Vegas, keith.lawler@unlv.edu

Andrew L. Hector
University of Southampton

Sylvain Petitgirard
University of Bayreuth

Ori Noked
Harvard University

Follow this and additional works at: https://digitalscholarship.unlv.edu/chem_fac_articles

 [next page for additional authors](#)
Part of the [Inorganic Chemistry Commons](#)

Repository Citation

Childs, C., Lawler, K. V., Hector, A. L., Petitgirard, S., Noked, O., Smith, J. S., Daisenberger, D., Bezacier, L., Jura, M., Pickard, C. J., Salamat, A. (2018). Covalency is Frustrating: La₂Sn₂O₇ and the Nature of Bonding in Pyrochlores under High Pressure–Temperature Conditions. *Inorganic Chemistry*, 57(24), 15051-15061. <http://dx.doi.org/10.1021/acs.inorgchem.8b01419>

This Article is protected by copyright and/or related rights. It has been brought to you by Digital Scholarship@UNLV with permission from the rights-holder(s). You are free to use this Article in any way that is permitted by the copyright and related rights legislation that applies to your use. For other uses you need to obtain permission from the rights-holder(s) directly, unless additional rights are indicated by a Creative Commons license in the record and/or on the work itself.

This Article has been accepted for inclusion in Chemistry and Biochemistry Faculty Publications by an authorized administrator of Digital Scholarship@UNLV. For more information, please contact digitalscholarship@unlv.edu.

Authors

Christian Childs, Keith V. Lawler, Andrew L. Hector, Sylvain Petitgirard, Ori Noked, Jesse S. Smith, Dominik Daisenberger, Lucile Bezacier, Marek Jura, Chris J. Pickard, and Ashkan Salamat

Covalency is Frustrating: $\text{La}_2\text{Sn}_2\text{O}_7$ and the Nature of Bonding in Pyrochlores under High Pressure–Temperature Conditions

Christian Childs,[†] Keith V. Lawler,^{*,‡,§} Andrew L. Hector,^{§,¶} Sylvain Petitgirard,[⊥] Ori Noked,[¶] Jesse S. Smith,[□] Dominik Daisenberger,[■] Lucile Bezacier,[○] Marek Jura,[●] Chris J. Pickard,^{△,▲} and Ashkan Salamat^{*,†}

[†]Department of Physics and Astronomy and HiPSEC, University of Nevada Las Vegas, Las Vegas, Nevada 89154, United States

[‡]Department of Chemistry and Biochemistry and HiPSEC, University of Nevada Las Vegas, Las Vegas, Nevada 89154, United States

[§]Department of Chemistry, University of Southampton, Southampton SO17 1BJ, United Kingdom

[⊥]Bayerisches GeoInstitut (BGI), University of Bayreuth, 95444 Bayreuth, Germany

[¶]Lyman Laboratory of Physics, Harvard University, Cambridge, Massachusetts 02138, United States

[□]High Pressure Collaborating Access Team at Advanced Photon Source, Geophysical Laboratory, Carnegie Institution of Washington, Argonne, Illinois 60439, United States

[■]Diamond Light Source Ltd., Didcot, Oxfordshire OX11 0DE, United Kingdom

[○]European Synchrotron Radiation Facility, BP 220, 38043 Grenoble, Cedex 9, France

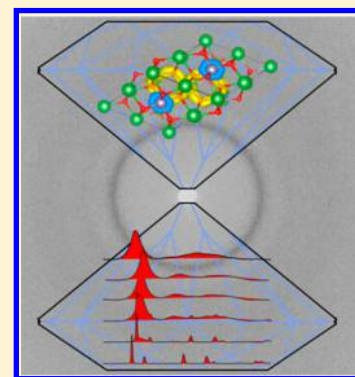
[●]ISIS, STFC, Harwell Innovation Campus, Didcot, Oxfordshire OX11 0QX, United Kingdom

[△]Department of Materials Science & Metallurgy, University of Cambridge, 27 Charles Babbage Road, Cambridge CB3 0FS, United Kingdom

[▲]Advanced Institute for Materials Research, Tohoku University, Sendai 980-8577, Japan

Supporting Information

ABSTRACT: Natural specimens of the pyrochlore ($\text{A}_2\text{B}_2\text{O}_7$) compounds have been found to retain foreign actinide impurities within their parent framework, undergoing metamictization to a fully amorphous state. The response to radionuclide decay identifies pyrochlore systems with having high radiation tolerance and tailored use in radioactive waste applications and radionuclide sequestration. High pressure is a powerful pathway to high density states and amorphization with parallels to radiation-induced processes. Here, $\text{La}_2\text{Sn}_2\text{O}_7$ is evaluated under extreme conditions via the combination of laser heating in a diamond anvil cell with X-ray diffraction and Raman spectroscopy. The measurements are supported by ab initio random structure searching and molecular dynamics calculations. A new ground state at 70 GPa is revealed, and high temperature annealing is fundamental to access its crystalline ground state and fully determine the structure. This crystalline phase ($P2_1/c$) retains its structural integrity during decompression and is fully recoverable to ambient conditions. The final state of the system is shown to be highly pathway dependent due to the covalent nature of the Sn–O bonding. The Tc pyrochlore, $\text{La}_2\text{Tc}_2\text{O}_7$, is analyzed for similarities in the bonding to determine the likelihood of an analogous pathway dependency to a final state.



INTRODUCTION

Pyrochlore oxides are a focus of intensive research, partly due to the large variety of physical and chemical properties that can be tuned by changes in composition.^{1–3} As a result, there are significant applications of these systems in many areas of technological interest.^{4–6} A strongly emerging area in materials-based research is the use of pyrochlore oxides as matrixes to sequester and immobilize radionuclides, particularly actinides and Gd produced in the nuclear fuel cycle.^{7–9} This interest is motivated by the chemical stability, low swelling, and high radiation tolerance of pyrochlore materials. Additionally, natural pyrochlore ores are known to have actinide impurities, and several actinide dioxides adopt the

related fluorite (CaF_2) structure.^{7,10} The properties of lanthanide-technetium pyrochlore oxides have also been investigated, as pyrochlore oxides may have use as a ⁹⁹Tc waste form.¹¹

Natural pyrochlore ores are known to undergo metamictization to a fully amorphous form as are the synthetic pyrochlore actinide and lanthanide immobilization materials.¹² The alpha decay events and the kinetic energy recoil the associated nuclei of most radioactive actinides and lanthanides release large amounts of energy (~5 MeV). That energy introduces defects

Received: May 23, 2018

Published: July 2, 2018

in the crystal lattice, leading to amorphization, swelling, and increased dissolution rates of the pyrochlore materials. The energy damage can be emulated in the laboratory via ion irradiation of samples.¹³ The decay events happen over the long half-lives of the radionuclides being sequestered, providing continuous radiation damage to the host matrix, altering the requirements for long-term immobilization. Storage of nuclear waste necessitates structural stability over the half-life of the radionuclides being stored. Therefore, it is important to fully understand the structural behavior and stability of all candidate waste forms, including controlled amorphization, to better design long-term storage solutions.

The archetypal pyrochlore oxide structure is a defect fluorite structure ($Fd\bar{3}m$) with $1/8$ th of the anion sites vacant and stoichiometry: $A_2B_2X_6Y$, $X = O^{2-}$, $Y = O^{2-}, OH^-, F^-$. The eight-coordinate A^{3+} and six-coordinate B^{4+} cation sites form edge-sharing coordination polyhedra whose shape change with composition and external constraints (e.g., pressure and temperature).⁷ The stability of the pyrochlore oxide is largely dependent on the ratio of the radii of the A-site and the B-site cations (r_A/r_B).¹⁴ The formation of the pyrochlore structure can be found in the cation radius ratio range between 1.46 ($Gd_2Zr_2O_7$) and 1.78 ($Sm_2Ti_2O_7$) under ambient conditions. The A-site cations are typically the nuclei to be sequestered, and the typical B-site cations and radii are Sn, 69 pm; Zr, 72 pm; and Ti, 60.5 pm. The cation radius ratio is also considered a good predictor of radiation tolerance because one of the main radiation damage mechanisms are cation antisite defects.¹⁵ These defects result in an A cation on the B sublattice or vice versa, and their associated energy cost is directly proportional to the difference in cation radii. A second main factor contributing to the stability of the pyrochlore structure is the electronic configuration, predominately of the B–O bond. It has been shown that zirconate pyrochlores exhibit better resistance to radiation damage than the titanates, attributed to the more ionic nature of Zr–O bonding.¹⁶ The ionicity of bonding with the typical B-site cations generally follows $Sn < Ti < Zr$.

The possibility of accessing high pressure pathways provides an alternative route to studying the structural stability of the pyrochlore structure with parallels to radiation-induced processes. High pressure conditions can introduce strain and defects into a crystal structure, raise its free energy, and give rise to structural and electronic transitions. If the kinetic energy required for a phase transition is too high, a material can often transition to an amorphous form. A number of pyrochlore compounds have been investigated under high pressure and have been shown to undergo pressure-induced amorphization (PIA).^{9,17,18} The pressure response and the occurrence of PIA are linked to the relative stabilizing forces in the solid-state structure of the pyrochlore oxide. While many pyrochlores exhibit PIA, there is no clear indication that the cation radius ratio is a reliable predictor for the existence of PIA. The cation radius ratio is also not a reliable predictor for the pressure of the critical onset of amorphization in the compounds that do exhibit PIA.¹⁹

$La_2Sn_2O_7$ adopts the archetypal $Fd\bar{3}m$ pyrochlore structure at ambient conditions and is well within the stability region ($r_A/r_B = 1.681$). The goal of studying this model non-radioactive pyrochlore material is twofold: first, to better understand the chemistry of the pyrochlore oxides, and second, to elucidate controlled pathways to amorphous forms or extreme conditions stable phases. These pathways can then be

applied as a pretreatment for radionuclide containing pyrochlores to achieve a waste form with a longer lifetime. An appropriate secondary containment system (glass, pressed ceramic, cement, etc.) could then be designed for the new waste form.

In this study, we investigate the structural behavior of $La_2Sn_2O_7$ under high temperature, high pressure, and high pressure–temperature conditions as outlined in Figure 1. The

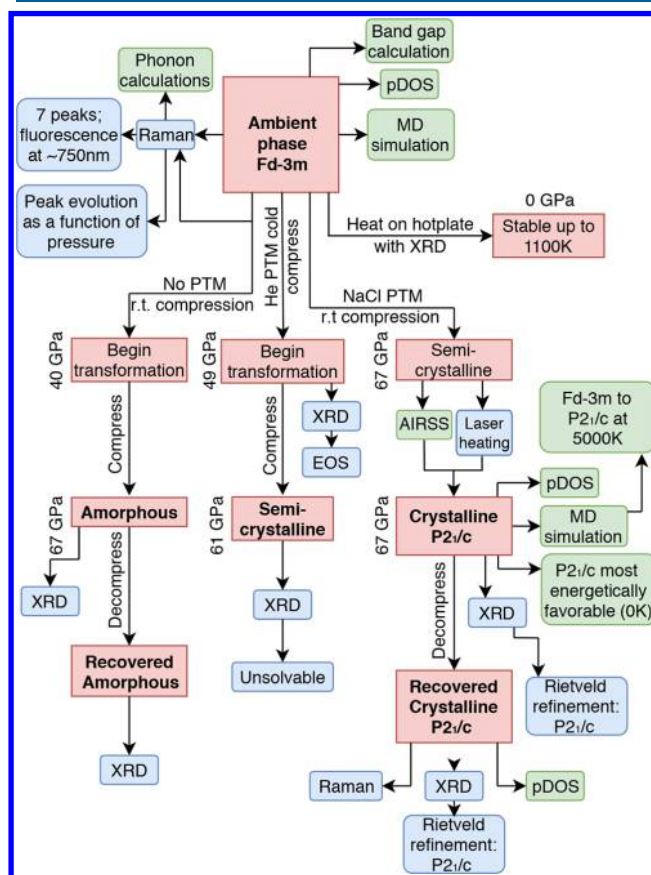


Figure 1. A summary of the various techniques and analysis undertaken: (blue) experimental work, (green) theoretical work, and (red) the various states in which the system is observed.

$Fd\bar{3}m$ structure exhibits a high degree of structural stability up to high temperatures. In contrast, the effects of strain/stress response on structural stability on the system shows pathways to two different recoverable final states. One pathway is to an amorphous form under nonhydrostatic conditions. The alternative pathway is a kinetically hindered first-order phase transition, preventing any reliable structural refinement. Laser-annealing at pressure produces a crystalline material that can be characterized using Rietveld refinement analysis.²⁰ First principles simulations support the experimental findings and provide an explanation for the stability regions and behaviors observed.

METHODS

Professor Neil Hyatt at the Department of Materials Science and Engineering, the University of Sheffield provided the $La_2Sn_2O_7$ sample. The sample was made by ball milling SnO_2 and La_2O_3 . Purity was confirmed by transmission electron microscopy (TEM), Raman, and X-ray diffraction (XRD). The $La_2Sn_2O_7$ sample was ground to a fine powder to ensure reliable averaging statistics from the powder diffraction experiments.

Isobaric heating was carried out on a Rigaku Smartlab (9 kW) diffractometer with Cu $K\alpha_1$ X-rays ($\lambda = 1.54056$ nm), parallel incident beam, θ - 2θ geometry, Dtex 1D detector, and Anton Paar HTK hot stage. The sample was heated under air, and temperature was measured using a thermocouple located just under the sample. The lattice parameters were extracted from the high temperature XRD data using Le Bail refinement.

Three high pressure compression runs were carried out. The first two runs were at room temperature using membrane-driven diamond anvil cells with 150 μm culets. Rhenium gaskets were indented to 20 μm with a starting hole size of 80 μm , and pressures were determined using ruby fluorescence methods. The first run was compressed with no pressure transmitting medium (PTM) up to 75 GPa at ID09a ($\lambda = 0.41570$ Å) of the European Synchrotron Radiation Facility (ESRF) using a MAR555 flatpanel detector. The second run was carried out using a He PTM for quasi-hydrostatic compression up to a final pressure of 61 GPa. The second run was investigated using angle-dispersive synchrotron X-ray diffraction at the high pressure beamline ECB P02.2 of PETRA III ($\lambda = 0.48281$ Å) with a Perkin-Elmer detector. The third run was loaded with a NaCl PTM, and the sample was split into four parts defined as quadrants. NaCl was used as the PTM to allow for laser heating due to its thermally insulating properties. The diamonds in the third run had 300 μm culets indented into a rhenium gasket to 31 μm . The sample chamber was approximately 120 μm wide. The sample was isothermally compressed to 67 GPa, and each quadrant was CO_2 laser-heated with a different amount of laser power (Table S1, Supporting Information). X-ray diffraction after laser-heating at high pressure was taken at HPCAT at the Advanced Photon Source (APS) in Argonne National Lab ($\lambda = 0.406626$ Å). The recovered laser-heated sample was investigated using angular-dispersive X-ray diffraction at Diamond Light Source ($\lambda = 0.42280$ Å). All diffraction data were integrated and then analyzed using Fit2D²¹ and GSAS.^{22,23} Indexing of the high pressure phase was conducted using the CRYSFIRE package, selecting solutions that gave reflections for all observable Bragg peaks and a high figure of merit.

Ab initio random structure searching (AIRSS)^{24–26} was performed at 70 GPa using the Perdew–Burke–Ernzerhof (PBE)²⁷ generalized gradient approximation (GGA) density functional^{28,29} in the plane wave code CASTEP.³⁰ The basis set cutoff energy was set to 450 eV using ultrasoft pseudopotentials with valence configurations of $5s^2 5p^6 6s^2 5d^1$ for La, $4d^{10} 5s^2 5p^2$ for Sn, and $2s^2 2p^4$ for O.³¹ A Γ -centered Monkhorst-Pack k -point grid with spacing $0.07 \times 2\pi$ Å⁻¹ was used to sample the Brillouin zone.³²

Additional ab initio simulations were done with the Vienna ab initio simulation package (VASP) version 5.4.1. These simulations used primitive (unless otherwise specified) representations of the unit cells and a k -point grid with $0.03 \times 2\pi$ Å⁻¹ resolution. The basis set cutoff energy was 600 eV using projector augmented wave (PAW)³³ pseudopotentials formulated for PBE GW with valence configurations of $5s^2 5p^6 6s^2 5d^1$ for La, $4d^{10} 5s^2 5p^2$ for Sn, $2s^2 2p^4$ for O, and $4s^2 4p^6 5s^2 5d^5$ for Tc.³⁴ Energy tolerances were set to 1×10^{-6} eV and force tolerances to 0.01 eV Å⁻¹. Molecular dynamics trajectories were propagated for 10 ps with 2 fs time steps by NpT ensemble Langevin dynamics.^{35–37} The first half of the simulation equilibrated the system, and statistics were taken over the second half of the simulation. The atoms had a friction coefficient of 5 ps⁻¹. The lattice degrees of freedom had a friction coefficient of 3 ps⁻¹ and fictitious mass of 100 amu.³⁵ The MD simulations used softer pseudopotentials (i.e. no La $5s^2$ or Sn $4d^{10}$), a 400 eV basis set cutoff energy, and a 1×10^{-5} eV energy tolerance.

RESULTS AND DISCUSSION

Properties of the Ambient Phase. Thermal amorphization is a common way to prepare materials as nuclear waste forms (i.e. vitrification into glasses). Therefore, a sample of $\text{La}_2\text{Sn}_2\text{O}_7$ was heated to 1050 K at 50 K intervals, while the structure was monitored by in situ X-ray diffraction to assess its thermal stability. The structure maintains a high degree of

crystallinity over the whole temperature range ($33.84 \leq wR_p \leq 36.94\%$) with a volume expansion of 1.90% (Figure S1 and Table S2, Supporting Information). The thermal volume expansion coefficient ($\alpha = 1/a_{300\text{K}} (da/dT)$) extracted from the data is 8.605×10^{-6} K⁻¹.³⁸ MD simulations corroborate the phase stability because a cubic unit cell of $\text{La}_2\text{Sn}_2\text{O}_7$ remains $Fd\bar{3}m$ up to 2000 K. The 2000 K MD simulation exhibits a slightly larger 6.81% volume expansion. $\text{La}_2\text{Sn}_2\text{O}_7$ should remain $Fd\bar{3}m$ until the melting point (>2000 °C) because these findings along with other measurements in the literature show a high thermal stability.^{39,40} The system clearly melts in an MD simulation at 5000 K, but the exact melting temperature was not probed. The hysteresis from such a small simulation box would prevent an accurate determination.^{41,42}

Having established the thermal stability of the ambient phase, the stability against compression needs to be evaluated. A previous study claims the ambient phase of $\text{La}_2\text{Sn}_2\text{O}_7$ is stable up to at least 17 GPa, with mostly crystalline $Fd\bar{3}m$ diffraction patterns up to 32 GPa.⁶ This has promising implications as a potential PIA pathway for pretreating pyrochlore radiowaste materials for long-term storage. However, there is a caveat to those results. A troublingly large amount (20–30%) of Sn disproportionated into a pure elemental phase as the material began to show a loss of crystallinity. The Sn disproportionation seemed to begin instantly upon compression. By 20 GPa, heavily distorted structure is reported. This is most likely a mix of $\text{La}_2\text{Sn}_2\text{O}_7$, Sn, and $\text{La}_2\text{Sn}_{2-x}\text{O}_7$ being fit as a single phase. To better understand the behavior of $\text{La}_2\text{Sn}_2\text{O}_7$ as a function of pressure, compression using both non- and quasi-hydrostatic conditions was investigated.

The initial compression pathway was carried out non-hydrostatically (no PTM) to induce amorphization through pressure. The ambient phase is retained up to ~ 40 GPa. A broad feature appears in the XRD pattern at 8–9 degrees after 40 GPa. The broad feature becomes more and more apparent upon further compression until the amorphization of the sample (Figure 2). By 75 GPa, the sample is completely amorphized; as expected, the amorphous XRD diffraction pattern shifts to higher diffraction angles (75 GPa S(Q) of the

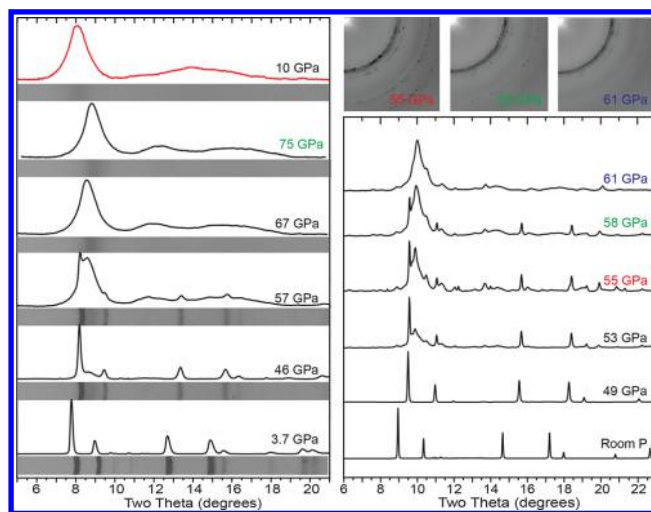


Figure 2. XRD stack plots of $\text{La}_2\text{Sn}_2\text{O}_7$ undergoing nonhydrostatic (no PTM, left, $\lambda = 0.41570$ Å) and quasi-hydrostatic (He PTM, right, $\lambda = 0.48281$ Å) compression. (right, top) Debye–Scherrer rings observed in quasi-hydrostatic compression.

amorphized sample in Figure S2, Supporting Information). The amorphous system can be decompressed down to ambient conditions. At ambient conditions, there is no significant change beyond the expected main diffraction peak relaxing lower in 2θ (Figure 2, top left curve). This can be interpreted as a large hysteresis or even more likely an irreversible phase transition. The recoverability of the amorphous form clearly demonstrates that nonhydrostatic compression is a means for PIA pretreatment of radiowaste pyrochlores. Although, the pressures here are somewhat high for high-throughput treatment of waste forms.

Sluggish pressure induced transition and amorphization in nonhydrostatic compression experiments can be related to the sample's microstructure evolution.⁴³ Pressure introduces strain and defects into the lattice that build up until the elevated free energy forces a structural change. Local domains within the sample, as well as the deviatoric stress due to the sample geometry, often mean that phase transitions can occur across a wide range of measured pressures. The deviatoric stress is exacerbated by pressure gradients within the sample. Moreover, a simplistic yet useful model for nucleation and growth of a new high pressure phase shows that the material is in an extreme nucleation dominant regime at the nonhydrostatic experimental conditions.⁴⁴ The critical radius for nucleation is very small in this regime. This scenario favors the creation of local nanocrystals that might be too small to be spatially coherent for X-ray diffraction, yielding the sample to be possibly X-ray amorphous. For the pyrochlore structure, it can also be predicted that such small nucleation centers will show increased propensity to become strictly amorphous, even to short-range order, given their energetic considerations.⁴⁵ More hydrostatic conditions can increase the critical radius for nucleation and decrease the concentration of defects and the associated strain energy, thereby enabling the nucleation of viable high pressure phase crystallites in the sample.

The nonhydrostatic conditions were initially assumed to be the cause for amorphization. Therefore, high pressure compression using helium as a PTM was carried out to evaluate whether the previously observed amorphization is an indication of a frustrated phase transition to a higher density crystalline phase. Helium remains a liquid under compression up to a pressure of 12.1 GPa at 300 K. He has the lowest bulk modulus, hence the highest compressibility, of any known solid.⁴⁶ It remains extremely soft with minimal nonhydrostatic stresses up to 150 GPa.⁴⁷ Use of such a soft PTM is vital to investigations of structural changes under pressure with the minimum degree of deviatoric stress. Under RT compression in He PTM, the ambient phase of $\text{La}_2\text{Sn}_2\text{O}_7$ is stable until a new phase emerges at 49.3 GPa. The transition goes to completion by 61 GPa (see Figure 2 (RHS)). Raman spectroscopy confirms the phase transition. The Raman band positions increase and intensities attenuate until all the bands disappear by 36 GPa (Figures S3 and S4, Supporting Information). After 36 GPa, the pattern is associated with an amorphous form's density of states.⁴⁸ However, the XRD data show a phase coexistence that makes it evident that the phase transition is kinetically hindered. The sluggish structural transition over such a pressure range leaves the new phase stressed and/or disordered as may be seen from the Debye–Sherrer rings (Figure 2). The phase coexistence of the high pressure and ambient systems confirms the first order nature of this transition. It is critical to note that due to the nature of the kinetically hindered first order transition, even using the softest

available PTM is not sufficient to allow access to a fully crystalline state. This type of kinetically hindered phase transition is seen in many other examples of pyrochlore materials under pressure.⁴³

As $Fd\bar{3}m$ $\text{La}_2\text{Sn}_2\text{O}_7$ remains highly crystalline under quasi-hydrostatic compression until 49.3 GPa, the equation of state (EoS) can be determined. The unit cell parameters extracted from the XRD data using Le Bail refinement (Figure S5 and Table S3, Supporting Information) show a 6.15% decrease in the cubic lattice constant from ambient pressure to 49.3 GPa. The third order Birch–Murnaghan (BM) EoS gives a bulk modulus of $K_0 = 183(4)$ GPa, $K_0' = 3.7(3)$, and a reference volume of $V_0 = 153.15(1) \text{ \AA}^3$.^{49,50} At first glance, the BM EoS appears to describe the expected response of the system during compression with a tight fit of the $V(P)$ data (Figure 3, inset).

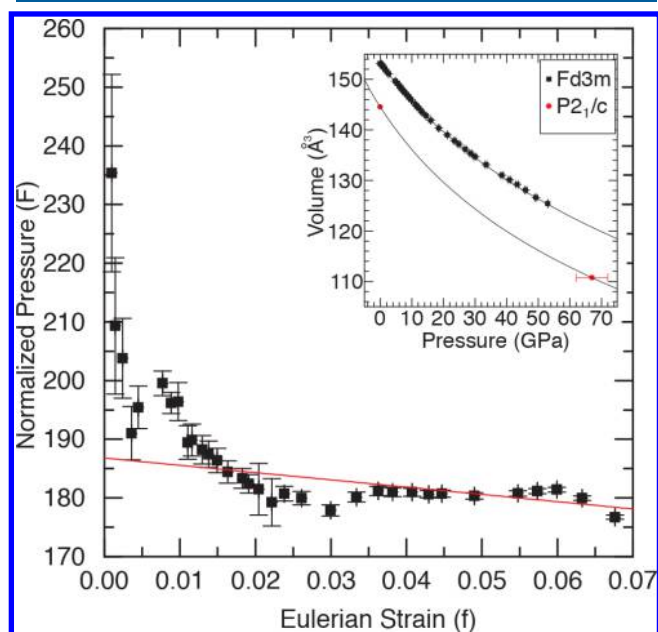


Figure 3. Compression of $\text{La}_2\text{Sn}_2\text{O}_7$ as a function of $F(f)$ and $V(P)$ (inset). Equation of state fits are shown as solid lines.

However, the compression data is very oscillatory around the fit to a linearized form of the BM relation. The linearized form uses the Eulerian-finite strain (f) vs normalized pressure (F), and it gives $K_0 = 188(3)$ and $K_0' = 3.8(2)$ from the y -axis intercept and gradient of the linear fit, respectively. Rietveld refinement can be attempted to monitor the displacement of the free oxygen position (i.e. X in the archetypal stoichiometry with crystallographic label O2). O2 is the only atom in the asymmetric cell with a coordinate not set by the crystal symmetry, and it is likely the origin of the oscillatory behavior. However, in this case and the initial heating experiment, reliable statistics could not be extracted due to the presence of the heavier cations and their significantly higher X-ray scattering contribution.

As O2 could not be monitored experimentally, the response of the internal geometry to strain was simulated by creating a series of structures at differing volumes. The volumes were created by changing the lattice constant of the ambient structure and optimizing the atomic coordinates. By comparing the geometric parameters before and after the optimization, only the O2 atoms moved. Every other atom stayed on its Wyckoff site. Parsing the material into the conventional

pyrochlore sublattices (A_2Y and B_2X_6) confines the distortions in the geometry to the Sn sublattice. All the bond and dihedral angles in the Sn sublattice would remain constant if O2 is kept fixed, yet Figure 4 shows they diverge from those values upon

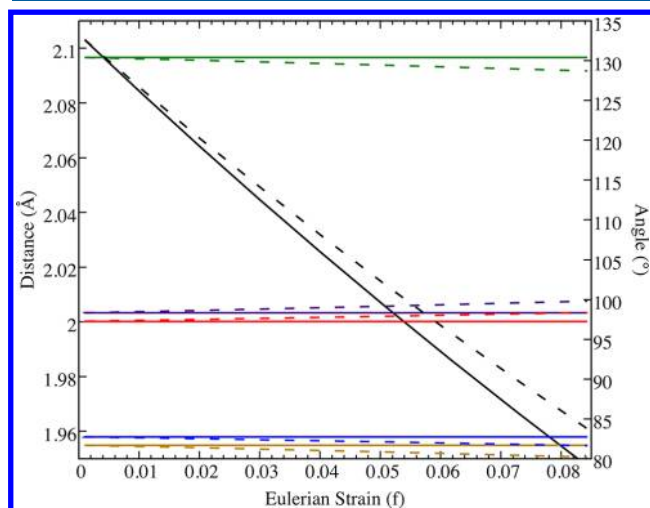


Figure 4. Change in geometries of the Sn sublattice obtained by reducing the volume of the cell, keeping atoms fixed (solid), and allowing the atomic positions to relax (dashed): (black) Sn–O2 length, (red) O2–Sn–O2 angle pointed into the Sn_4O_6 tetrahedral cages, (blue) O2–Sn–O2 angle pointed away from the cages, (green) Sn–O2–Sn angle, (purple) the dihedral angle between the basal plane and the axis of the SnO_6 octahedra pointed into the cages, and (gold) the dihedral angle pointed away from the cages.

compression. In a perfectly regular octahedron, the O–Sn–O bond angles and the dihedral angles between the basal planes and the primary axes would all be 90° . Even without compression, the SnO_6 octahedra are irregular. This irregularity only increases upon compression. The picture that arises is that the SnO_6 octahedra are twisting and compressing the Sn_4O_6 tetrahedral cages while their outward facing angles shrink to accommodate. Similar monotonic distortions from regularity are also observed in the LaO_8 cuboids. The combined effects of these rotations with the internal stresses preventing them in a real, nonannealed material is the cause of the observed oscillations in $F(f)$.

The resistance to compression of the Sn–O bond and the decrease of the Sn–O–Sn angle signal a covalent nature to the bonding in the Sn sublattice, the metal–oxygen–metal angle in compounds is known to be a marker of the covalency of the bond.^{51,52} A strong overlap of Sn s states and O2 p states at the bottom of the valence band around -6 eV exists in the site and angular momentum projected density of states for $Fd\bar{3}m$ $La_2Sn_2O_7$ (Figure S6, Supporting Information). Inspection of the band decomposed charge density shows 6 bands that are clearly a linear combination of Sn–O bonding orbitals wrapping around the Sn_4O_6 tetrahedral cages (Figure 5). All the other bands in the valence band appear to be linear combinations of O 2p lone pair orbitals, although those closest in energy to the Sn–O2 covalent bands show a polarization toward the Sn atoms (Figure S7, Supporting Information). There is also an overlap between La p states and O1 s states around -12 eV. However, inspection of the band decomposed charge densities does not show signs of covalency (Figure S8, Supporting Information). The La–O overlap is just a fortuitous energetic overlap of semivalent atomic states. The

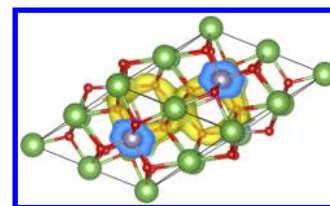


Figure 5. $La_2Sn_2O_7$ (Fdm). Representative charge density of a Sn–O covalent bonding band. The colors are: (green) La, (red) O, (gray) Sn, and (yellow/blue) the charge density isosurfaces.

bonding in the system is ionic between La and O and at least partially covalent between Sn and O2. In a three-center covalent bond between a metal–oxygen–metal unit, one of the metal–oxygen bonds disproportionates into an oxygen lone pair, while the other bond smears out over all three atomic centers.^{53,54} This provides a bond order of 0.50 for each metal–oxygen connection. There are 6 strongly covalent bands in $La_2Sn_2O_7$'s primitive cell for 24 Sn–O2 connections, an apparent bond order of 0.25. This means that twice as many bond–lone pair disproportionations have occurred than in a three-center covalent bond, or that some of the bands that visually appear to be linear combinations of oxygen lone pair orbitals may actually be part of the covalent network. Either way, the oxygens in the Sn sublattice have more ionic character than if they had single or three-center covalent bonds to the Sn atoms.

High Pressure Crystalline Phase. The kinetic hindrance of the phase transition at 61 GPa, even in a helium PTM, prevents any reliable indexing of the unit cell of the newly accessed high density phase based on the quasi-hydrostatic compression data. AIRSS was employed to help identify the unknown phase. The structure searches made use of space group symmetry and allowed up to 4 formula units per unit cell. The only constraints placed on the generated structures were minimum interatomic distances to prevent sampling unreasonable structures: O–O 2.53 Å, O–Sn 1.96 Å, O–La 2.31 Å, Sn–Sn 3.26 Å, Sn–La 3.29 Å, and La–La 3.65 Å. AIRSS identified three possible, energetically viable solutions: $P2_1/c$, 0 meV; $C2/c$, 105 meV; and $Pbcn$, 177 meV (Figure S9, Supporting Information). However, the quality of the XRD pattern is insufficient to permit a reliable match even with the AIRSS solutions. Our inability to index the new phase makes the need to thermally anneal this (or any) kinetically hindered structural phase transition quite clear, independent of the choice of PTM.

To that end, an alternative type of sample loading was prepared to test different thermal annealing conditions while in the thermodynamic stability region of the new high density phase. The top inset in Figure 6 shows the quadrant layout of the $La_2Sn_2O_7$ loading in a DAC at 67 GPa in a NaCl PTM. Each quadrant was laser heated with increased power density and duration (Table S1, Supporting Information). The stack plot in Figure 6 reveals the corresponding XRD patterns. There is a clear evolution of crystallinity with the peak shapes sharpening with stronger annealing conditions. In quadrant 1 (lowest power and duration), most of the features are from the NaCl PTM. The NaCl features persist in the other XRD patterns but become less dominant as features from the sample take precedence. Laser annealing at or above 3.9 MW/cm², quadrants 2–4, produces a crystalline sample with a varying degree of crystallinity. The crystallinity increases with temperature. The highest intensity (quadrant 4, 8.0 MW/cm² for a

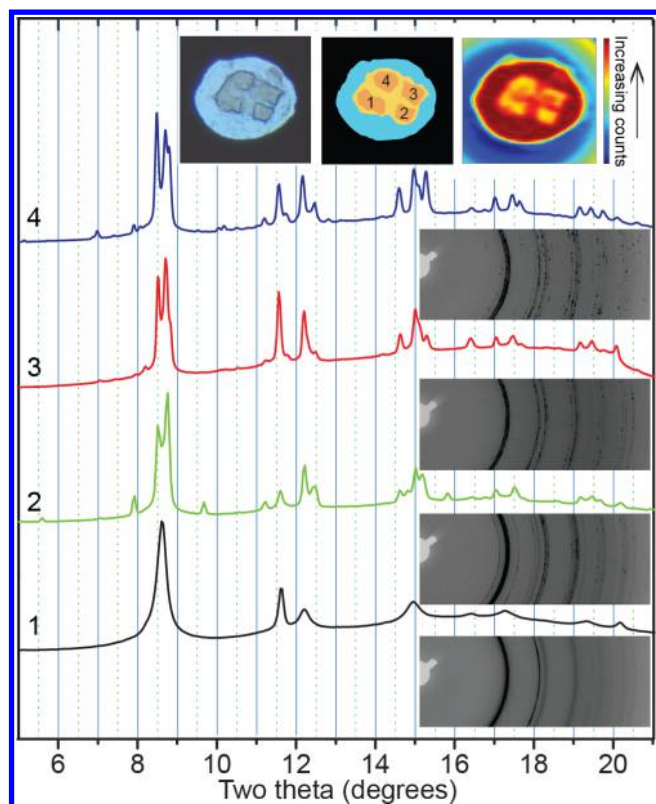


Figure 6. Four quadrant laser heated sample at 67 GPa. (top) Photos of the DAC loading with quadrant index (middle) and X-ray transmission profile (right). The XRD patterns in the stack plot correspond to the quadrant of the same number. Heating increased with quadrant number.

total of 775 s) produces the most crystalline XRD pattern. The Raman spectra for each quadrant was featureless prior to heating. Only a single Raman peak appears at 870 cm^{-1} (at pressure) upon heating. Decomposition/disproportionation is a concern in high temperature experiments, but there is no evidence of elemental species or metal oxides in the XRD and Raman data. The pyrochlore remains intact even at the most extreme temperatures and pressures, so the previous report of a build-up of elemental Sn upon compression is most likely an ill-explained artifact of their experimental approach.⁶

There is a distinctive improvement in XRD quality of the post laser heated XRD pattern compared to the quasi-hydrostatically XRD pattern (Figure 2 (right) and Figure 6), demonstrating that laser heating enabled the sample to overcome the kinetic barriers and access the crystalline thermodynamic ground state. Overcoming those barriers enables true structure determination. The 67 GPa, post laser heating XRD pattern can be Rietveld refined ($wR_p = 4.5\%$ and $R_p = 2.1\%$) using the lowest energy solution, $P2_1/c$, from the AIRSS calculations (Figure 7, $a = 8.3376(4)\text{ \AA}$, $b = 5.3657(6)\text{ \AA}$, $c = 9.7935(5)\text{ \AA}$, $\beta = 90.381(5)^\circ$). Rietveld refinement reveals the same $P2_1/c$ phase (Figure 7, $a = 9.39975(9)$, $b = 5.75590(2)$, $c = 10.68544(7)\text{ \AA}$, $\beta = 89.9341(1)^\circ$, $wR_p = 2.0\%$ and $R_p = 1.1\%$) when the sample is decompressed back down to ambient pressure. The quality of the data enabled full refinement of all the atomic position in the cell (Table S4, Supporting Information). This includes the anion positions, thus providing a reliable structure model of the new phase.

During the laser heating experiments, it can be estimated that quadrant 4 achieved a temperature in excess of 2500 K.

This demonstrates a robust thermal stability of the $P2_1/c$ phase quite similar to the $Fd\bar{3}m$ phase at ambient conditions. MD simulations show that a single unit cell of the $P2_1/c$ phase remains crystalline at 70 GPa and 5000 K with a 7.17% volume expansion (Figure 8). The volume expands through a dilation of the b - and c -crystallographic axes coupled with a slight contraction of the a -axis. More remarkably, a cubic unit cell of the $Fd\bar{3}m$ phase at 70 GPa and 5000 K appears to transform into the $P2_1/c$ phase (Figure 8), albeit without perfect crystalline ordering. A primitive unit cell of the $Fd\bar{3}m$ phase transforms into a cell resembling the $C2/c$ AIRSS solution at 70 GPa and 5000 K. A primitive $Fd\bar{3}m$ cell contains only 22 atoms, so it cannot access the 44 atom $P2_1/c$ cell. In contrast, a cubic unit cell of the $Fd\bar{3}m$ phase at 70 GPa and 2000 K remains in the same phase. This shows that the small box size is artificially stabilizing the $Fd\bar{3}m$ phase compared to experiment. However, a large enough thermal kick overcomes the artificial stabilization and allows the system to access one of the more favorable high pressure polymorphs. Though the length and time scales of the MD simulations are too small to properly show nucleation or melting,⁵⁵ they are of sufficient quality to confirm the following: the $Fd\bar{3}m$ phase transforms into the $P2_1/c$ phase at high pressure and temperature, and the $P2_1/c$ phase is thermally stable up to at least the experimental temperatures (by comparison the $Fd\bar{3}m$ phase melts by 5000 K at 0 GPa).

As in the $Fd\bar{3}m$ phase, the site and angular momentum projected density of states for $P2_1/c$ $\text{La}_2\text{Sn}_2\text{O}_7$ at 70 GPa shows a strong overlap of Sn s states and O p states for the 8 bands at the bottom of the valence band (Figure S10, Supporting Information). The band decomposed charge densities for these bands show a covalency between the Sn and O. Unlike the covalency in the $Fd\bar{3}m$ phase, the Sn–O covalent network does not connect with all the oxygen atoms in the SnO_6 octahedra. The network is square bipyramidal with one oxygen per octahedra not connected (i.e. no density between the Sn and O). These noncovalent oxygens are the same atoms in each band, and they have the smallest density overlap (labeled O2 and O5) with the Sn. They are also the only oxygen atom in a SnO_6 octahedra that is not connected to another Sn but rather is a part of 3 La atoms' polyhedra. That connectivity is clearly driving their bonding to be predominantly ionic, like O1 in the $Fd\bar{3}m$ phase. Eight bands describing 8 octahedra each with 5 Sn–O connections gives an apparent Sn–O bond order of 0.20, lower than that in the $Fd\bar{3}m$ phase. Also like the $Fd\bar{3}m$ phase, the band below the valence band exhibits density overlap between La and O atoms. However, in this case it is more clearly just an energetic overlap of semivalent states. The charge densities of the bands are even more obviously atom localized than in the $Fd\bar{3}m$ phase (Figure 9). The ambient $P2_1/c$ structure has the same electronic structure as the 70 GPa structure (Figure S11, Supporting Information), and the perseverance of the Sn–O covalent network provides an explanation as to why the phase is easily recoverable to ambient conditions.

Considering these results, it is now clear why this material exhibits a kinetically hindered first order phase transition. It is transitioning from one covalent network about the Sn atoms to another. The Sn octahedra in the $P2_1/c$ phase are even less regular than in the $Fd\bar{3}m$ phase. The Sn–O distances now vary for each atom, and each of the three planes containing 4 O and the Sn are no longer flat. The oscillations in the $F(f)$ EoS (Figure 3) are now more easily explained as the resistance of

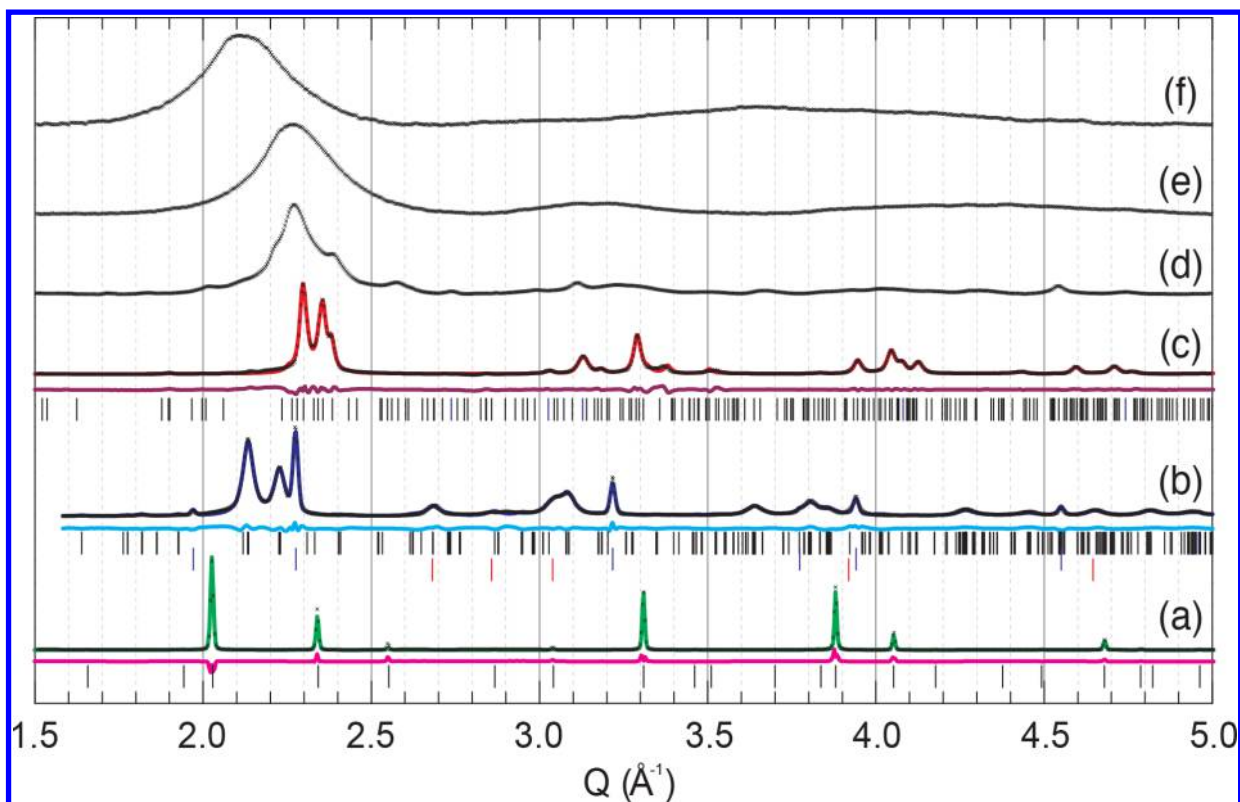


Figure 7. A comparison of XRD patterns of the various states of the sample investigated, from bottom: (a) ambient phase, (b) recovered $P2_1/c$: ($a = 9.39975(9)$, $b = 5.75590(2)$, $c = 10.68544(7)$ Å, $\beta = 89.9341(1)^\circ$), (c) $P2_1/c$ postlaser-heating at 67 GPa ($a = 8.3376(4)$, $b = 5.3657(6)$, $c = 9.7935(5)$ Å, $\beta = 90.381(5)^\circ$), (d) quasi-hydrostatically compressed at 61 GPa, (e) nonhydrostatically compressed at 75 GPa, and (f) recovered nonhydrostatically compressed.

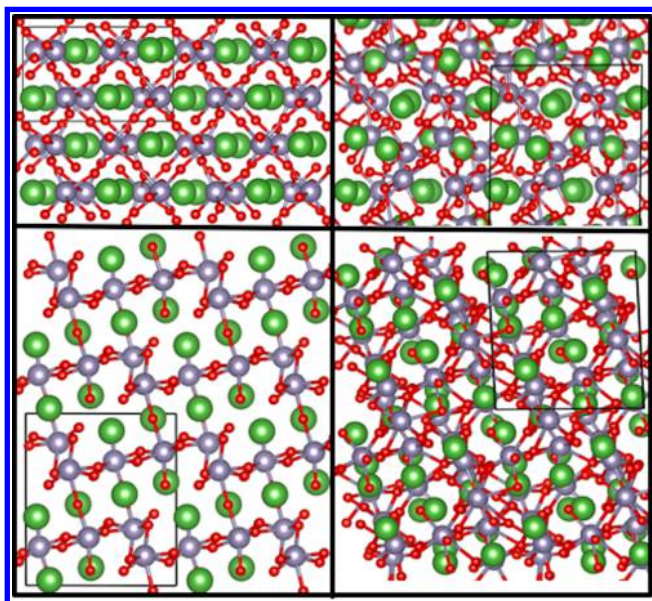


Figure 8. Final snapshots of the MD simulations at 70 GPa and 5000 K of a $P2_1/c$ (left) unit cell along (001) , (top) and (100) , (bottom), and an $Fd\bar{3}m$ (right) unit cell along (100) , (top) and (001) , (bottom). La–O connectivities not shown, and the colors are the same as in Figure 5.

the covalent network to compression coupled with the pressure induced phase coexistence and its accompanying transformation of the character of the covalent network, leading to anisotropic strains. The covalent to covalent translation is the source of the frustration in the phase

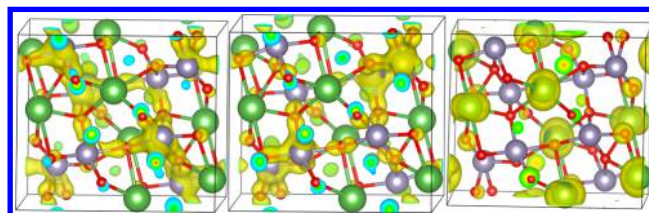


Figure 9. (left, middle) Representative charge density of Sn–O covalent bonding bands in $P2_1/c$ $\text{La}_2\text{Sn}_2\text{O}_7$. (right) A representative band where the La and O densities of state exhibit overlap. The colors are the same as those in Figure 5.

transformation and is also the likely cause behind the previously observed frustrated phase transformations in other pyrochlores.⁴³ By comparison to previous studies, we can assert that the covalency in pyrochlores should decrease in the order $\text{Sn} > \text{Ti} > \text{Zr}$. The leading cause of amorphization is antisite defects and a sublattice with increased covalent character should more strongly resist those defects. Therefore, Sn pyrochlores should be the more stable and tolerant to radiation damage crystalline materials, especially in their high pressure annealed phases.

Implications for Tc Pyrochlores. Despite all the interest in actinide and lanthanide pyrochlores, there has only been one study to date investigating technetium pyrochlore oxides.¹¹ However, Tc pyrochlore oxides represent an interesting candidate waste form material. For instance, unlike actinides and lanthanides, ⁹⁹Tc is a weak β emitter (293 keV), so the material would experience a significantly reduced amount of radiation-induced amorphization.⁵⁶ Tc is only known to

present as Tc(IV) and Tc(VII) in solid-state oxides.⁵⁷ Tc would need to occupy the B-site as Tc(IV), as shown to be the case in lanthanide (but not La) Tc pyrochlores. Tc(IV) species have generally low volatility and are also much more readily retained chemically compared to higher valent oxo species.⁵⁸ Tc(IV) is also the most environmentally immobile form. Immobilizing ⁹⁹Tc(IV) in a stable material would provide an ideal long-term storage solution. It would also eliminate the issue of upward of 70% of the Tc volatilizing away during vitrification at ~1100 °C into a borosilicate glass, the current strategy for a ⁹⁹Tc waste form at the Hanford site.^{56,59} Some groups have attempted to trap Tc(IV) as a dopant in iron-oxide materials such as magnetite, Fe₃O₄.⁵⁸ When a Tc-doped magnetite sample is heated to 600 °C, the surface Tc oxidizes and volatilizes off. By 700 °C, even the bulk Tc migrates to the surface, oxidizes, and volatilizes off. The inability of that material to retain Tc(IV) significantly reduces its utility for vitrification or storage in geologic repositories.

A thermally stable material that better incorporates Tc(IV) would be an ideal waste form. We have already demonstrated that La₂Sn₂O₇ is a thermally stable material to upward of 2000 °C in both of its phases. It would be quite significant if La₂Tc₂O₇ is analogous to La₂Sn₂O₇. There is reason to believe that is the case given the similarities between Tc and Sn: Tc is known to form covalent bonds with O,^{54,60,61} the covalent radius of Sn is 1.40 Å and 1.38 for Tc Å,^{14,62} and the ionic radius for octahedral Sn(IV) is 0.69 Å compared to 0.645 Å for Tc(IV). The electronic structure of *Fd* $\bar{3}m$ La₂Tc₂O₇ at 0 GPa and *P2*₁/*c* La₂Tc₂O₇ at 70 GPa can be compared to that of La₂Sn₂O₇ to test for a similarity between the materials. The Tc pyrochlore structures were obtained by substituting Tc for Sn and allowing the structure to fully relax. Tc(IV) will have three d electrons that are not ionic or bonding with the ligands. As the Tc atoms are surrounded by ligand, those *d*³ electrons may localize entirely on-atom. To account for the potential localization, the rotationally invariant single parameter Hubbard DFT+U correction (*U*_{eff} = 4.0 eV)^{63,64} was applied to the Tc d states along with a high spin guess. Ferromagnetic (FM) ordering was used because it is the simplest spin ordering for on-atom localization. While other spin orderings may have lower energy, the FM solution's geometry and electronic structure will be similar enough to make general conclusions.

The partial density of states for *Fd* $\bar{3}m$ La₂Tc₂O₇ at 0 GPa and *P2*₁/*c* La₂Tc₂O₇ at 70 GPa show that the Tc to Sn analogy holds true (Figures S12 and S13, Supporting Information). The key difference between the two systems is the nature of the B-site d electrons. The 4d electrons in Sn are semivalent, whereas in Tc they sit above the oxygen lone pairs at the top of the valence band. Both structures adopted the anticipated atom localized *d*³ electrons (*S* = 3/2). Other magnetic solutions (i.e. *S* = 1/2 and diamagnetic) indicative of itinerant d electrons exist, but they are all higher in energy than the *S* = 3/2 state. More importantly, both symmetries exhibit similar covalent bonding bands to their Sn counterparts (Figure 10). The Tc-O covalent network wraps around tetrahedra of the Tc sublattice in the *Fd* $\bar{3}m$ structure. The *P2*₁/*c* bonding network is also similar, except the states have split between being oriented equatorially (Figure 10, right) and being oriented axially. This division likely arises from an energetic splitting of the Tc d orbitals participating in the bonding (i.e. *t*_{2g} and *e*_g). The presence of similar covalent networks in both phases of La₂Tc₂O₇ leads us to believe the similarity will extend to the

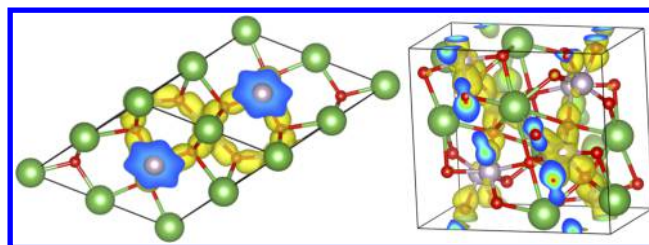


Figure 10. Representative charge density of Tc–O covalent bonding bands in La₂Tc₂O₇: (left) *Fd* $\bar{3}m$ at 0 GPa and (right) *P2*₁/*c* at 70 GPa. The colors are the same as those in Figure 5.

other properties of the material (like the desirable thermal stability), making it a promising waste form.

The electronic structure of *Fd* $\bar{3}m$ La₂Tc₂O₇ at 0 GPa without DFT+U is identical except for the energy gap between the occupied spin-up Tc d states and unoccupied spin-down d states decreasing from ~2.0 to 0.1 eV. This confirms the correct nature of the DFT+U electronic structures. The energy gap between the occupied spin-up Tc d states and unoccupied spin-down d states in *P2*₁/*c* La₂Tc₂O₇ at 70 GPa is 0.5 eV with DFT+U. This follows the traditional route of a system's band gap closing as a function of pressure. The *S* = 3/2 FM states cannot be found without the DFT+U correction, and in general, nonmagnetic states are more favorable than *S* = 1/2 states. The value of *U*_{eff} was chosen based on a study of another Tc(IV) oxide, TcO₂, so it should be reliable and transferable to this problem. However, this behavior raises interesting questions about the phase diagram. Is there a high pressure transition to a semimetallic or fully metallic state? Where do metallic transitions happen relative to the structural phase transition into the *P2*₁/*c* phase? How are the metallic transitions affected by changing the identity of the A-site cation? The answer to those questions could have great ramifications on the preparation of Tc pyrochlores and their long-term behavior in a repository.

CONCLUSION

Several different methods and approaches were undertaken to provide an in-depth understanding of La₂Sn₂O₇, its responses to temperature and pressure, and the underlying chemistry behind it. Beginning with the ambient conditions characterization of the starting material, this work reveals a high purity single phase material with a marked thermal stability owing to the covalent network covering the Sn sublattice. Non-hydrostatic compression leads to pressure-induced amorphization, while quasi-hydrostatic conditions reveal La₂Sn₂O₇ undergoing a kinetically hindered first order phase transition beginning around 49.3 GPa. It can be deduced that the kinetic hindrance combined with no PTM leads to deviatoric stresses which cause pressure-induced amorphization. Laser annealing is required to fully transform compressed La₂Sn₂O₇ into its high pressure phase. Structure searching, molecular dynamics, and Rietveld refinement identify the high pressure phase as *P2*₁/*c* symmetry. Inspection of the electronic structure of the *P2*₁/*c* phase reveals a covalent network about the Sn atoms that differs from that of the *Fd* $\bar{3}m$ phase. The large change required to facilitate the transition between the two different bonding networks is the leading cause of the kinetic hindrance. On the other hand, the persistence of the bonding in the *P2*₁/*c* high pressure phase to ambient conditions is a likely reason behind its recoverability. It is interesting to consider which

previously reported pyrochlores would exhibit similar behavior and the other phases that would be observed if they were re-examined under high pressure with laser annealing.

This work aimed to explore structure properties in pyrochlores to consider the implications for their improved usage as waste forms for radionuclides. $\text{La}_2\text{Tc}_2\text{O}_7$ and $\text{La}_2\text{Sn}_2\text{O}_7$ have very similar electronic structures in both the $Fd\bar{3}m$ and $P2_1/c$ phases. This provides a new candidate waste material that could trap Tc in its environmentally immobile Tc(IV) state and simultaneously be robust against pressure and temperature. Nonhydrostatic compression shows promise as a route for preparing initially amorphous waste forms for other radionuclides. However, the 61 GPa amorphization pressure is likely too high for practical preparations. The choice of the A- and B-site cations (or mixed compositions) will need to be carefully considered to balance the robustness of the covalent network and the mechanical work required for either pressure-induced amorphization or accessing a crystal-line phase more tolerant of extreme conditions. The build-up of radiation damage at different pressures will be a vital additional input into the system's energy landscape. High pressure experiments on ion irradiated samples need to be done to further understand the structural stability of nuclear waste forms. The introduction of temperature to radioactive samples under pressure can potentially reveal even more insights. The combination of these techniques will unravel the interplay between pressure and radiation induced structural transformations.

■ ASSOCIATED CONTENT

Supporting Information

The Supporting Information is available free of charge on the ACS Publications website at DOI: 10.1021/acs.inorgchem.8b01419.

XYZ laser heating profiles; XRD patterns; Raman spectra; refined lattice constants and atomic positions; band structure plots; partial densities of state; band-decomposed charge density plots; and AIRSS structural solutions at 70 GPa (PDF)

■ AUTHOR INFORMATION

Corresponding Authors

*E-mail: salamat@physics.unlv.edu.

*E-mail: keith.lawler@unlv.edu.

ORCID

Keith V. Lawler: 0000-0003-1087-5815

Andrew L. Hector: 0000-0002-9964-2163

Notes

The authors declare no competing financial interest.

■ ACKNOWLEDGMENTS

We thank Neil C. Hyatt from the University of Sheffield for the sample and Michael Hanfland of European Synchrotron Radiation Facility for beam time at ID09a. The authors gratefully acknowledge computational resources and support provided by the UNLV National Supercomputing Institute. This research was sponsored by the National Nuclear Security Administration under the Stewardship Science Academic Alliances program through DOE Cooperative Agreement DE-NA0001982. Portions of this work were performed at HPCAT (Sector 16), Advanced Photon Source (APS),

Argonne National Laboratory. HPCAT operations are supported by DOE-NNSA under Award DE-NA0001974 and DOE-BES under Award DE-FG02-99ER45775, with partial instrumentation funding by NSF. A.P.S. is supported by DOE-BES under Contract DE-AC02-06CH11357. C.J.P. acknowledges financial support from the Engineering and Physical Sciences Research Council (EPSRC) of the UK under Grant EP/P022596/1. C.J.P. is also supported by the Royal Society through a Royal Society Wolfson Research Merit Award.

■ REFERENCES

- (1) Subramanian, M. A.; Aravamudan, G.; Subba Rao, G. V. Oxide Pyrochlores — A Review. *Prog. Solid State Chem.* **1983**, *15* (2), 55–143.
- (2) Glerup, M.; Nielsen, O. F.; Poulsen, F. W. The Structural Transformation from the Pyrochlore Structure, A2B2O_7 , to the Fluorite Structure, AO_2 , Studied by Raman Spectroscopy and Defect Chemistry Modeling. *J. Solid State Chem.* **2001**, *160* (1), 25–32.
- (3) Abe, R.; Higashi, M.; Zou, Z.; Sayama, K.; Abe, Y. Photocatalytic Water Splitting into H_2 and O_2 over $\text{R}_2\text{Ti}_2\text{O}_7$ ($\text{R} = \text{Y}$, Rare Earth) with Pyrochlore Structure. *Chem. Lett.* **2004**, *33* (8), 954–955.
- (4) Sardar, K.; Petrucco, E.; Hiley, C. I.; Sharman, J. D. B.; Wells, P. P.; Russell, A. E.; Kashtiban, R. J.; Sloan, J.; Walton, R. I. Water-Splitting Electrocatalysis in Acid Conditions Using Ruthenate-Iridate Pyrochlores. *Angew. Chem., Int. Ed.* **2014**, *53* (41), 10960–10964.
- (5) Ryzhkin, I. A. Magnetic Relaxation in Rare-Earth Oxide Pyrochlores. *J. Exp. Theor. Phys.* **2005**, *101* (3), 481–486.
- (6) Zhao, Y.; Li, N.; Xu, C.; Li, Y.; Zhu, H.; Zhu, P.; Wang, X.; Yang, W. Abnormal Pressure-Induced Photoluminescence Enhancement and Phase Decomposition in Pyrochlore $\text{La}_2\text{Sn}_2\text{O}_7$. *Adv. Mater.* **2017**, *29* (34), 1701513.
- (7) Ewing, R. C.; Weber, W. J.; Lian, J. Nuclear Waste Disposal—Pyrochlore (A2B2O_7): Nuclear Waste Form for the Immobilization of Plutonium and “Minor” Actinides. *J. Appl. Phys.* **2004**, *95* (11), 5949–5971.
- (8) Wang, S. X.; Begg, B. D.; Wang, L. M.; Ewing, R. C.; Weber, W. J.; Kutty, K. V. G. Radiation Stability of Gadolinium Zirconate: A Waste Form for Plutonium Disposition. *J. Mater. Res.* **1999**, *14* (12), 4470–4473.
- (9) Salamat, A.; McMillan, P. F.; Firth, S.; Woodhead, K.; Hector, A. L.; Garbarino, G.; Stennett, M. C.; Hyatt, N. C. Structural Transformations and Disorder in Zirconolite ($\text{CaZrTi}_2\text{O}_7$) at High Pressure. *Inorg. Chem.* **2013**, *52* (3), 1550–1558.
- (10) Atencio, D.; Andrade, M. B.; Christy, A. G.; Giere, R.; Kartashov, P. M. THE PYROCHLORE SUPERGROUP OF MINERALS: NOMENCLATURE. *Can. Mineral.* **2010**, *48* (3), 673–698.
- (11) Hartmann, T.; Alaniz, A.; Poineau, F.; Weck, P. F.; Valdez, J. A.; Tang, M.; Jarvinen, G. D.; Czerwinski, K. R.; Sickafus, K. E. Structure Studies on Lanthanide Technetium Pyrochlores as Prospective Host Phases to Immobilize 99technetium and Fission Lanthanides from Effluents of Reprocessed Used Nuclear Fuels. *J. Nucl. Mater.* **2011**, *411* (1–3), 60–71.
- (12) Ringwood, A. E.; Kesson, S. E.; Ware, N. G.; Hibberson, W.; Major, A. Immobilisation of High Level Nuclear Reactor Wastes in SYNROC. *Nature* **1979**, *278* (5701), 219–223.
- (13) Lang, M.; Zhang, F.; Zhang, J.; Wang, J.; Schuster, B.; Trautmann, C.; Neumann, R.; Becker, U.; Ewing, R. C. Nanoscale Manipulation of the Properties of Solids at High Pressure with Relativistic Heavy Ions. *Nat. Mater.* **2009**, *8* (10), 793–797.
- (14) Shannon, R. D. Revised Effective Ionic Radii and Systematic Studies of Interatomic Distances in Halides and Chalcogenides. *Acta Crystallogr., Sect. A: Cryst. Phys., Diffraction, Theor. Gen. Crystallogr.* **1976**, *32* (5), 751–767.
- (15) Minervini, L.; Grimes, R. W.; Sickafus, K. E. Disorder in Pyrochlore Oxides. *J. Am. Ceram. Soc.* **2000**, *83* (8), 1873–1878.
- (16) Trachenko, K.; Pruneda, J. M.; Artacho, E.; Dove, M. T. How the Nature of the Chemical Bond Governs Resistance to

Amorphization by Radiation Damage. *Phys. Rev. B: Condens. Matter Mater. Phys.* **2005**, *71* (18), 184104.

(17) Zhang, F. X.; Saxena, S. K. Structural Changes and Pressure-Induced Amorphization in Rare Earth Titanates RE₂Ti₂O₇ (RE: Gd, Sm) with Pyrochlore Structure. *Chem. Phys. Lett.* **2005**, *413* (1–3), 248–251.

(18) Zhang, F. X.; Lian, J.; Becker, U.; Wang, L. M.; Hu, J.; Saxena, S.; Ewing, R. C. Structural Distortions and Phase Transformations in Sm₂Zr₂O₇ Pyrochlore at High Pressures. *Chem. Phys. Lett.* **2007**, *441* (4–6), 216–220.

(19) Salamat, A.; Hector, A. L.; McMillan, P. F.; Ritter, C. Structure, Bonding, and Phase Relations in Bi₂Sn₂O₇ and Bi₂Ti₂O₇ Pyrochlores: New Insights from High Pressure and High Temperature Studies. *Inorg. Chem.* **2011**, *50* (23), 11905–11913.

(20) Salamat, A.; Fischer, R. A.; Briggs, R.; McMahon, M. I.; Petitgirard, S. In Situ Synchrotron X-Ray Diffraction in the Laser-Heated Diamond Anvil Cell: Melting Phenomena and Synthesis of New Materials. *Coord. Chem. Rev.* **2014**, *277–278*, 15–30.

(21) Hammersley, A. P.; Svensson, S. O.; Hanfland, M.; Fitch, A. N.; Häussermann, D. Two-Dimensional Detector Software: From Real Detector to Idealised Image or Two-Theta Scan. *High Pressure Res.* **1996**, *14* (4–6), 235–248.

(22) Larson, A. C.; Von Dreele, R. B. General Structure Analysis System (GSAS). *Los Alamos Natl. Lab. Rep. LAUR 86–748* **2000**.

(23) Toby, B. H. EXPGUI, a Graphical User Interface for GSAS. *J. Appl. Crystallogr.* **2001**, *34* (2), 210–213.

(24) Pickard, C. J.; Needs, R. J. High-Pressure Phases of Silane. *Phys. Rev. Lett.* **2006**, *97* (4), 045504.

(25) Pickard, C. J.; Needs, R. J. Ab Initio Random Structure Searching. *J. Phys.: Condens. Matter* **2011**, *23* (5), 053201.

(26) Ab Initio Random Structure Searching Software 0.9.0 <http://www.mtg.msm.cam.ac.uk/Codes/AIRSS> (accessed Feb 6, 2018).

(27) Perdew, J. P.; Burke, K.; Ernzerhof, M. Generalized Gradient Approximation Made Simple. *Phys. Rev. Lett.* **1996**, *77* (18), 3865–3868.

(28) Rajagopal, A. K.; Callaway, J. Inhomogeneous Electron Gas. *Phys. Rev. B* **1973**, *7* (5), 1912–1919.

(29) Kohn, W.; Sham, L. J. Self-Consistent Equations Including Exchange and Correlation Effects*. *Phys. Rev.* **1965**, *140* (4A), 1133–1138.

(30) Clark, S. J.; Segall, M. D.; Pickard, C. J.; Hasnip, P. J.; Probert, M. I. J.; Refson, K.; Payne, M. C. First Principles Methods Using CASTEP. *Z. Kristallogr. - Cryst. Mater.* **2005**, *220* (5/6), 567–570.

(31) Vanderbilt, D. Soft Self-Consistent Pseudopotentials in a Generalized Eigenvalue Formalism. *Phys. Rev. B: Condens. Matter Mater. Phys.* **1990**, *41* (11), 7892–7895.

(32) Monkhorst, H. J.; Pack, J. D. Special Points for Brillouin-Zon Integrations. *Phys. Rev. B* **1976**, *13* (12), 5188–5192.

(33) Blöchl, P. E. Projector Augmented-Wave Method. *Phys. Rev. B: Condens. Matter Mater. Phys.* **1994**, *50* (24), 17953–17979.

(34) Lejaeghere, K.; Bihlmayer, G.; Björkman, T.; Blaha, P.; Blugel, S.; Blum, V.; Caliste, D.; Castell, I. E.; Clark, S. J.; Dal Corso, A.; de Gironcoli, S.; Deutsch, T.; Dewhurst, J. K.; Di Marco, I.; Draxl, C.; Du ak, M.; Eriksson, O.; Flores-Livas, J. A.; Garrity, K. F.; Genovese, L.; Giannozzi, P.; Giantomassi, M.; Goedecker, S.; Gonze, X.; Granas, O.; Gross, E. K. U.; Gulans, A.; Gygi, F.; Hamann, D. R.; Hasnip, P. J.; Holzwarth, N. A. W.; Iu an, D.; Jochym, D. B.; Jollet, F.; Jones, D.; Kresse, G.; Koepnick, K.; Kucukbenli, E.; Kvashnin, Y. O.; Loch, I. L. M.; Lubeck, S.; Marsman, M.; Marzari, N.; Nitzsche, U.; Nordstrom, L.; Ozaki, T.; Paulatto, L.; Pickard, C. J.; Poelmans, W.; Probert, M. I. J.; Refson, K.; Richter, M.; Rignanese, G.-M.; Saha, S.; Scheffler, M.; Schlipf, M.; Schwarz, K.; Sharma, S.; Tavazza, F.; Thunstrom, P.; Tkatchenko, A.; Torrent, M.; Vanderbilt, D.; van Setten, M. J.; Van Speybroeck, V.; Wills, J. M.; Yates, J. R.; Zhang, G.-X.; Cottenier, S. Reproducibility in Density Functional Theory Calculations of Solids. *Science (Washington, DC, U. S.)* **2016**, *351* (6280), aad3000–aad3001.

(35) Allen, M. P.; Tildesley, D. J. *Computer Simulation of Liquids*; Oxford University Press: New York, 1991.

(36) Parrinello, M.; Rahman, A. Crystal Structure and Pair Potentials: A Molecular-Dynamics Study. *Phys. Rev. Lett.* **1980**, *45* (14), 1196–1199.

(37) Parrinello, M.; Rahman, A. Polymorphic Transitions in Single Crystals: A New Molecular Dynamics Method. *J. Appl. Phys.* **1981**, *52* (12), 7182–7190.

(38) Radhakrishnan, A. N.; Prabhakar Rao, P.; Mahesh, S. K.; Vaisakhan Thampi, D. S.; Koshy, P. Role of Bond Strength on the Lattice Thermal Expansion and Oxide Ion Conductivity in Quaternary Pyrochlore Solid Solutions. *Inorg. Chem.* **2012**, *51* (4), 2409–2419.

(39) Wang, S.; Zhou, G.; Lu, M.; Zhou, Y.; Wang, S.; Yang, Z. Synthesis and Characterization of Lanthanum Stannate Nanoparticles. *J. Am. Ceram. Soc.* **2006**, *0*, 060613004617008.

(40) Kong, L.; Karatchevtseva, I.; Blackford, M. G.; Scales, N.; Triani, G. Aqueous Chemical Synthesis of Ln₂Sn₂O₇ Pyrochlore-Structured Ceramics. *J. Am. Ceram. Soc.* **2013**, *96* (9), 2994–3000.

(41) Eshet, H.; Khaliullin, R. Z.; Kühne, T. D.; Behler, J.; Parrinello, M. Microscopic Origins of the Anomalous Melting Behavior of Sodium under High Pressure. *Phys. Rev. Lett.* **2012**, *108* (11), 115701.

(42) Zhang, W.; Peng, Y.; Liu, Z. Molecular Dynamics Simulations of the Melting Curve of NiAl Alloy under Pressure. *AIP Adv.* **2014**, *4* (5), 057110.

(43) Zhang, F. X.; Lang, M.; Becker, U.; Ewing, R. C.; Lian, J. High Pressure Phase Transitions and Compressibilities of Er[Sub 2]Zr[Sub 2]O[Sub 7] and Ho[Sub 2]Zr[Sub 2]O[Sub 7]. *Appl. Phys. Lett.* **2008**, *92* (1), 011909.

(44) Yamanaka, T.; Nagai, T.; Tsuchiya, T. Mechanism of Pressure-Induced Amorphization. *Z. Kristallogr. - Cryst. Mater.* **1997**, *212* (6), 401–410.

(45) Piot, L.; Le Floch, S.; Cornier, T.; Daniele, S.; Machon, D. Amorphization in Nanoparticles. *J. Phys. Chem. C* **2013**, *117* (21), 11133–11140.

(46) Takemura, K.; Dewaele, A. Isothermal Equation of State for Gold with a He-Pressure Medium. *Phys. Rev. B: Condens. Matter Mater. Phys.* **2008**, *78* (10), 104119.

(47) Dewaele, A.; Loubeyre, P. Pressurizing Conditions in Helium-Pressure-Transmitting Medium. *High Pressure Res.* **2007**, *27* (4), 419–429.

(48) Shuker, R.; Gammon, R. W. Raman-Scattering Selection-Rule Breaking and the Density of States in Amorphous Materials. *Phys. Rev. Lett.* **1970**, *25* (4), 222–225.

(49) Murnaghan, F. D. The Compressibility of Media under Extreme Pressures. *Proc. Natl. Acad. Sci. U. S. A.* **1944**, *30* (9), 244–247.

(50) Birch, F. Finite Elastic Strain of Cubic Crystals. *Phys. Rev.* **1947**, *71* (11), 809–824.

(51) Weigend, F.; Ahlrichs, R. Balanced Basis Sets of Split Valence, Triple Zeta Valence and Quadruple Zeta Valence Quality for H to Rn: Design and Assessment of Accuracy. *Phys. Chem. Chem. Phys.* **2005**, *7* (18), 3297.

(52) Dixon, D. A.; Gole, J. L. Description of the Ground State Electronic Structures of Cu₂O, Cu₂S, Ag₂O and Ag₂S. *Chem. Phys. Lett.* **1992**, *189* (4–5), 390–394.

(53) Ramsden, C. A. Non-Bonding Molecular Orbitals and the Chemistry of Non-Classical Organic Molecules. *Chem. Soc. Rev.* **1994**, *23* (2), 111.

(54) Lawler, K. V.; Childs, B. C.; Mast, D. S.; Czerwinski, K. R.; Sattelberger, A. P.; Poineau, F.; Forster, P. M. Molecular and Electronic Structures of M₂O₇ (M = Mn, Tc, Re). *Inorg. Chem.* **2017**, *56* (5), 2448–2458.

(55) Khaliullin, R. Z.; Eshet, H.; Kühne, T. D.; Behler, J.; Parrinello, M. Nucleation Mechanism for the Direct Graphite-to-Diamond Phase Transition. *Nat. Mater.* **2011**, *10* (9), 693–697.

(56) Darab, J. G.; Smith, P. A. Chemistry of Technetium and Rhenium Species during Low-Level Radioactive Waste Vitrification. *Chem. Mater.* **1996**, *8*, 1004–1021.

(57) Schwochau, K. *Technetium*; Wiley-VCH: Weinheim, 2000.

(58) Lee, M.-S.; Um, W.; Wang, G.; Kruger, A. A.; Lukens, W. W.; Rousseau, R.; Glezakou, V.-A. Impeding $^{99}\text{Tc}(\text{IV})$ Mobility in Novel Waste Forms. *Nat. Commun.* **2016**, *7*, 12067.

(59) Rard, J. A. Current Status of the Thermodynamic Data for Technetium and Its Compounds and Aqueous Species. *J. Nucl. Radiochem. Sci.* **2005**, *6* (3), 197–204.

(60) Childs, B. C.; Lawler, K. V.; Braband, H.; Mast, D. S.; Bigler, L.; Stalder, U.; Peterson, D. R.; Jansen, A.; Forster, P. M.; Czerwinski, K. R.; Alberto, R.; Sattelberger, A. P.; Poineau, F. The Nature of the Technetium Species Formed During the Oxidation of Technetium Dioxide with Oxygen and Water. *Eur. J. Inorg. Chem.* **2018**, *2018* (9), 1137–1144.

(61) Lawler, K. V.; Childs, B. C.; Czerwinski, K. R.; Sattelberger, A. P.; Poineau, F.; Forster, P. M. Unraveling the Mystery of “Tech Red” – a Volatile Technetium Oxide. *Chem. Commun.* **2018**, *54* (10), 1261–1264.

(62) *CRC Handbook of Chemistry and Physics*, 97th ed.; Haynes, W. M., Ed.; CRC Press/Taylor & Francis: Boca Raton, FL, 2016.

(63) Dudarev, S. L.; Botton, G. A.; Savrasov, S. Y.; Humphreys, C. J.; Sutton, A. P. Electron-Energy-Loss Spectra and the Structural Stability of Nickel Oxide: An LSDA+U Study. *Phys. Rev. B: Condens. Matter Mater. Phys.* **1998**, *57* (3), 1505–1509.

(64) Taylor, C. D. Oxidation of Technetium Metal as Simulated by First Principles. *J. Phys. Chem. C* **2014**, *118* (19), 10017–10023.